Dealing with Uncertainty in Diffusion Tensor MR Data

PETER J. BASSER[a,*] AND SINISA PAJEVIC[b]
[a]Section on Tissue Biophysics & Biomimetics, LIMB, NICHD, National Institutes of Health, 13 South Drive, Bldg. 13, Rm. 3W16, Bethesda, Maryland 20892-5772, USA
[b]Mathematical and Statistical Computing Laboratory, CIT, National Institutes of Health, Bethesda, Maryland 20892-5772, USA

(Received 28 March 2003 and in revised form 23 July 2003)

Abstract. This paper explains how radio frequency (RF) background noise produces uncertainty in measured diffusion tensor MRI (DT-MRI) data, how this noise can be modeled, and how its effects can be mitigated. DT-MRI data are derived from a series of magnitude diffusion-weighted images (DWI) in which RF noise is rectified. A new Gaussian distribution is proposed that describes the variability of the estimated diffusion tensor, $\boldsymbol{D}$, in an ideal experiment in which RF noise is the only artifact present. We show how to improve the design of DT-MRI experiments by requiring that the statistical distribution of $\boldsymbol{D}$ be independent of the laboratory coordinate system. Non-parametric empirical methods of analyzing uncertainty in DT-MRI experiments are also described. Monte Carlo simulations are useful in designing and interpreting DT-MRI experiments. Bootstrap methods help us measure the true variability of $\boldsymbol{D}$ (and quantities derived from it), and assess the quality of DT-MRI data. Matrix Perturbation techniques predict how the uncertainty in $\boldsymbol{D}$ propagates to its eigenvalues and eigenvectors. A method for obtaining a continuous diffusion tensor field from the measured discrete noisy DT-MRI data also reduces the uncertainty of $\boldsymbol{D}$ and quantities derived from it. Finally, we describe schemes that use wavelets to remove noise from DWI and DT-MRI data while preserving boundaries between different tissue regions. Collectively, these parametric and nonparametric methods provide a unified statistical framework to improve the design of DT-MRI experiments and their subsequent analysis.

INTRODUCTION TO DT-MRI

What is DT-MRI?

The MR measurement of an effective or apparent diffusion tensor of water, $\boldsymbol{D}$,[1] and the analysis and display of the information it contains in each voxel is called Diffusion Tensor MRI (DT-MRI) .[2] It is now well established that the MR measurement of $\boldsymbol{D}$ in tissues can provide unique biologically and clinically relevant information that is not available from other imaging modalities. This information includes parameters that help characterize tissue composition, the physical properties of tissue constituents, tissue microstructure, and its architectural organization. Moreover, this measurement is performed noninvasively, without exogenous contrast agents.

Characterizing Diffusion in Biological Systems

In tissues such as brain gray matter, where the voxel-averaged apparent diffusivity (measured using typical dimensions of 2 mm × 2 mm × 2 mm) is largely independent of the orientation of the tissue (i.e., macroscopically isotropic), it is usually sufficient to characterize water diffusion characteristics with a single (scalar) apparent diffusion coefficient (ADC). However, in skeletal and cardiac muscle[3–5] and in white matter[6–8] the voxel-averaged ADC depends upon the orientation of the tissue. In these macroscopically anisotropic media, a single scalar ADC cannot describe the orientation-dependent water mobility. The next most complex

*Author to whom correspondence should be addressed. E-mail: pjbasser@helix.nih.gov

model of diffusion that can describe anisotropic diffusion replaces the scalar diffusion coefficient with a symmetric effective or apparent diffusion *tensor* of water, $\boldsymbol{D}$ (e.g., see ref 9).

Biological and Clinical Applications of DT-MRI

Since the apparent diffusivity of water molecules is sensitive to changes in its local environment, $\boldsymbol{D}$ acts as a probe of tissue architecture. This makes DT-MRI attractive for studying changes in white matter structure and organization in a variety of clinical investigations. These include applications in acute[10–12] and chronic[13] ischemia, multiple sclerosis,[14] Alzheimer's disease,[15] amyotrophic lateral sclerosis,[16,17] alcoholism,[18,19] dyslexia,[20] epilepsy,[21,22] HIV,[23,24] schizophrenia,[25,26] tumors,[27,28] and Wallerian degeneration.[29] DT-MRI has also been used to study normal aging from neurodevelopment[30,31] through childhood[32] and adult life.[33–35]

Physical Underpinnings of Diffusion Tensor NMR and MRI

Torrey[36] first incorporated anisotropic translational diffusion to the Bloch (magnetization transport) equations[37] as an additional mechanism that causes attenuation of the NMR signal. Analytical solutions to this equation followed for freely diffusing species during a spin echo experiment[38] and, later, for diffusion in restricted geometries (e.g., refs 39–41). About a decade after its introduction, Stejskal and Tanner solved the Bloch–Torrey equation[42] for the case of free, anisotropic diffusion in the principal frame of reference. However, the Stejskal–Tanner formula is not generally applicable for measuring $\boldsymbol{D}$ using NMR or MRI methods for several reasons.

First, the Stejskal–Tanner formula relates a time-dependent diffusion tensor, $\boldsymbol{D}(t)$, to the NMR signal. Thus, one must define the relationship between $\boldsymbol{D}(t)$ and $\boldsymbol{D}$.[1] Second, in the era preceding the development of MRI, in which Stejskal–Tanner developed their formalism, it was always assumed that a homogeneous anisotropic sample could be physically oriented within the magnet so that its principal axes could be aligned with the laboratory coordinate system. After the invention of MRI, however, this assumption was no longer tenable. Materials under study, like turbid tissues, were often heterogeneous media whose "fiber" or principal axes were generally not known a priori and could vary from place to place within the sample. Thus, a general framework had to be developed to measure the entire diffusion tensor (both its diagonal and off-diagonal elements) in the laboratory frame of reference[1] and its variation within an imaging volume.[2]

In DT-MRI, we define $\boldsymbol{D}$ as a function of $\boldsymbol{D}(t)$[1] analogous to the way Tanner defined an apparent diffusion coefficient from the time-dependent scalar diffusivity.[43] Then, we relate $\boldsymbol{D}$ to the measured NMR echo according to:

$$\ln\left(\frac{A(\boldsymbol{b})}{A(\boldsymbol{b}=\boldsymbol{0})}\right) = -\sum_{i=1}^{3}\sum_{j=1}^{3} b_{ij}\, D_{ij} =$$
$$-\left(b_{xx}D_{xx} + 2\,b_{xy}D_{xy} + 2\,b_{xz}D_{xz} + b_{yy}D_{yy} + 2\,b_{yz}D_{yz} + b_{zz}D_{zz}\right) =$$
$$-Trace(\boldsymbol{b} : \boldsymbol{D}) \qquad (1)$$

where $A(\boldsymbol{b})$ and $A(\boldsymbol{b} = \boldsymbol{0})$ are the echo magnitudes of the diffusion-weighted and non-diffusion-weighted signals, respectively, and b_{ij} is a component of the symmetric b-matrix, $\boldsymbol{b}$.[1] The b-matrix is calculated for each diffusion-weighted image (DWI), and summarizes the attenuating effect of *all* gradient waveforms applied in all three directions, x, y, and z.[44-46] Finally, $\boldsymbol{D}$ is estimated from a series of DWIs using eq 1.[1] The measurement of $\boldsymbol{D}$ is inherently statistical: We use each DWI and its corresponding b-matrix to statistically estimate $\boldsymbol{D}$ using multivariate linear regression[1] of eq 1 as described in ref 1.

Derived Parameters Produced by DT-MRI

Intrinsic quantitative parameters can be extracted from diffusion-tensor MRI data that characterize distinct features describing the size, shape, orientation, or pattern of root mean square (rms) displacement profiles within an imaging volume. Scalar parameters, derived from the diagonal *and* off-diagonal elements of $\boldsymbol{D}(\boldsymbol{x})$ with $\boldsymbol{x} = (x,y,z)$ can be displayed as an image that exhibits different distinct features of the diffusion tensor field and their distribution within the imaging volume.[47] These quantities are rotationally invariant, i.e., independent of the orientation of the tissue structures, the patient's body within the MR magnet, the applied diffusion sensitizing gradients, and the choice of the laboratory coordinate system in which the components of the diffusion tensor and magnet field gradients are measured.[2,48] Some examples are Trace($\boldsymbol{D}$), which is proportional to the orientationally-averaged intrinsic diffusivity (or "mean ADC"), and the eigenvalues of $\boldsymbol{D}$, which are the principal diffusivities along the local principal axes of $\boldsymbol{D}$.

Other information can be obtained from the eigenvectors of $\boldsymbol{D}$, which define the orientations of the local principal axes. For instance, color maps that indicate the local fiber-tract orientation are created by combining information contained in the eigenvector associated with the large principal diffusivity and a measure of diffusion anisotropy.[49–52] Fiber-tract trajectories can be constructed from $\boldsymbol{D}$ data by generating streamlines that follow the local direction of maximum apparent diffusivity (e.g., see refs 2, 53–65).

The definition and physical interpretation of useful MR parameters derived from ***D***, such as the Trace(***D***), as well as measures of diffusion anisotropy, have been reviewed elsewhere, e.g., ref 66. Moreover, several review articles and book chapters have covered many different aspects of diffusion tensor MRI.[67–71] This article is concerned primarily with how noise affects DT-MRI data.

THEORY

Parametric Statistical Approaches to Model Variability in DT-MRI Experiments

Johnson noise present in the radio-frequency (RF) detection system is the most basic source of variability in diffusion MR data. This MR signal is rectified when producing magnitude DWIs that are used in eq 1 to estimate ***D***. The noise characteristics of these rectified signals have been well characterized by Henkelman,[72] and the noise distribution is known to be Rician,[73]

$$p(m,a,\sigma) = \frac{m}{\sigma^2}\, e^{-\frac{m^2+a^2}{2\sigma^2}}\, I_0\!\left(\frac{ma}{\sigma}\right) \qquad (2)$$

where $I_0(x)$ is the modified Bessel function of the first kind, m is the magnitude, a is the parameter that controls the mean of the distribution, and σ is the standard deviation of the experimental noise. Since the components of ***D*** are estimated from noisy DWI using regression analysis (generally multivariate linear regression of the log-linearized DW magnitude signals[i]), the appropriate parametric distribution of noise in ***D*** data within a voxel is a multivariate Gaussian.[74] This is because for signal-to-noise (S/N) ratios greater than 3, the Rician distribution is well approximated by a normal distribution with mean $\sqrt{a^2+m^2}$, and variance σ^2, which is the variance of the signal in each of the quadrature channels.[72,73] Even though the relationship between the magnitude of the NMR signal and the components of ***D*** is nonlinear, and arriving at an analytical expression for the noise distribution of the individual diffusion tensor elements is problematic, regression analysis is usually performed using a large number of independent DW signals (i.e., > 7). In this case, the Central Limit Theorem (even for small S/N ratios) ensures that the distribution of the elements of ***D*** will be a multivariate normal distribution:[ii]

$$p\left(x\,|\,\bar{\mu},M\right) = \frac{|M|}{(2\pi)^2}\, e^{-\frac{1}{2}(x-\bar{\mu})^T M (x-\bar{\mu})} \qquad (3)$$

in which the six independent components of ***D*** are written as a 6-dimensional random vector $x = \{D_{xx},D_{yy},D_{zz},D_{xy},D_{xz},D_{yz}\}$. This distribution has two parameters: a 6×6 precision (or inverse covariance) matrix, ***M***, and a 6-dimensional mean vector, $\bar{\mu} = \{\bar{D}_{xx},\bar{D}_{yy},\bar{D}_{zz},\bar{D}_{xy},\bar{D}_{xz},\bar{D}_{yz}\}$. Above, $|\boldsymbol{M}|$ is the determinant of ***M***. Figure 1 displays Monte Carlo simulated DT-MRI data in which the distribution of each element of ***D*** is shown in a representative white matter compartment in the brain. Such simulations, described below in more detail, are one way to verify the accuracy and applicability of parametric statistical models.

The result that the components of ***D*** are normally distributed is an important one. First, one can immediately derive the parametric distribution of some useful tensor-derived quantities, such as Trace(***D***):[75]

$$p(Trace(\boldsymbol{D})) = \frac{1}{\sqrt{2\pi\sigma_T^{\,2}}}\, \exp\!\left(-\frac{(Trace(\boldsymbol{D})-\hat{\mu})^2}{2\sigma_T^{\,2}}\right) \qquad (4)$$

in which $\hat{\mu} = \bar{D}_{xx} + \bar{D}_{yy} + \bar{D}_{zz}$, and $\sigma_T^2 = \sigma_{xxxx}^2 + \sigma_{yyyy}^2 + \sigma_{zzzz}^2 + 2\sigma_{xxyy}^2 + 2\sigma_{yyzz}^2 + 2\sigma_{xxzz}^2$, where, for example, σ_{xxyy}^2

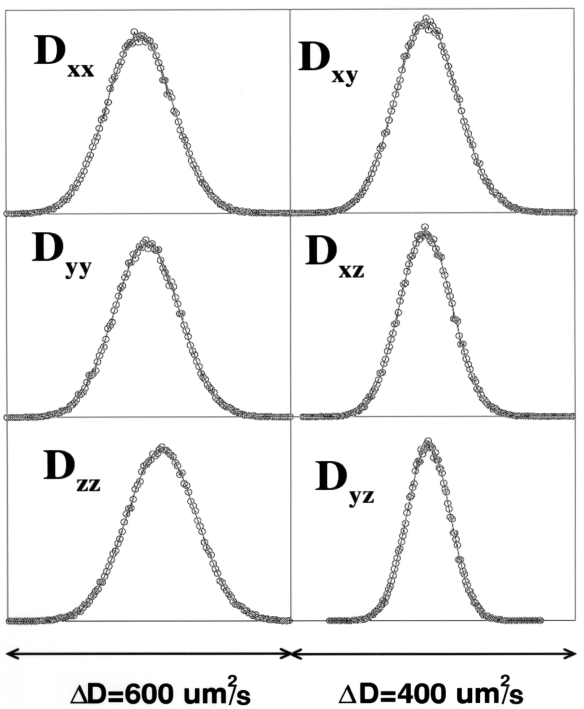

Fig. 1. Monte Carlo simulated DT-MRI data in which the Gaussian distribution of each element of ***D*** is shown in a representative brain white matter compartment. Taken from ref 74.

[i] Multivariate linear regression is just one of a number of techniques, including nonlinear regression and singular-value decomposition, that could be used to estimate ***D*** from the echo data.

[ii] This result applies for both linear and nonlinear regression due to a property of least-square minimization.

is the covariance of D_{xx} and D_{yy}. Figure 2 shows an empirical estimate of the distribution of Trace(***D***) in three representative human brain compartments, including white matter, gray matter, and cerebrospinal fluid (CSF). This result was obtained using another empirical statistical method, described below, called "bootstrap".

Moreover, this multivariate normal distribution formalism allows us to use powerful hypothesis tests to address many problems in DT-MRI data analysis that previously were treated only in an ad hoc manner.

However, writing ***D*** as a vector, ***x***, fails to preserve certain intrinsic algebraic relationships among its elements and their geometric relationships with the laboratory coordinate system in which the tensor elements are measured. For example, algebraic operations naturally performed on ***D*** (e.g., decomposing it into its eigenvalues and eigenvectors), or geometric operations (e.g., projecting it along a particular direction, or applying an affine transformation to it), are unwieldy when ***D*** is written as a vector.

Additionally, the form of ***M*** offers no insight into the way noise or features of the experimental design affect the distribution of the diffusion tensor elements, or that of tensor-derived quantities. The democratic way in which the multivariate (vector) representation treats tensor components makes it difficult to appreciate their unique roles. A new tensor-variate normal distribution, whose form we recently proposed, preserves the algebraic and geometric structure of the tensor random variable, and thus our ability to perform various algebraic and geometric operations on it.[76]

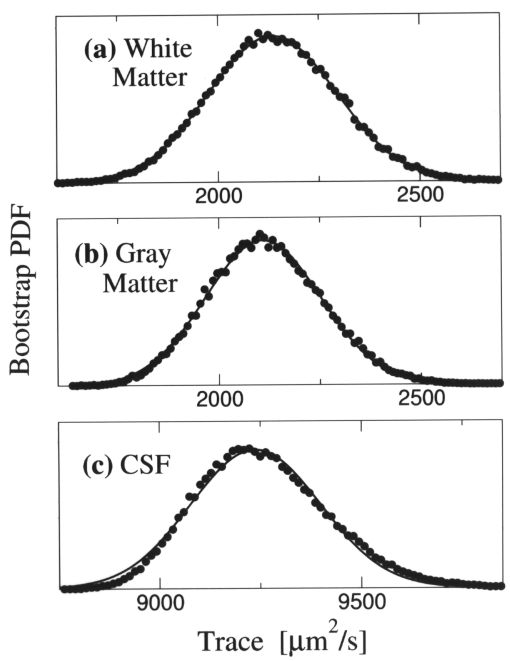

Fig. 2. Bootstrap estimate of the distribution of Trace(***D***) for representative voxels in brain gray matter, white matter, and cerebrospinal fluid (CSF). In an experiment in which artifacts are well controlled, the distribution in representative voxels should be Gaussian.

Tensor-variate Normal Distribution of ***D***

The key idea motivating this new distribution is intuitive. Just as vector-valued data are written in vector form in the exponent of a multivariate normal distribution,[77] 2nd (and higher)-order tensors should be written in tensor form in the exponent of a *tensor*-variate normal distribution. Specifically, the scalar exponent of the multivariate normal probability density function (pdf) in eq 2, $p(\boldsymbol{x})$, contains a quadratic form, $\boldsymbol{x}^T \boldsymbol{M}\, \boldsymbol{x}$, of an N-dimensional normal random vector, ***x***, and the precision matrix, ***M***. In tensor parlance, $\boldsymbol{x}^T \boldsymbol{M}\, \boldsymbol{x}$ is a *scalar contraction*—a linear operation that reduces one or more higher order tensors to a 0th-order tensor (or scalar). In this case, $x_i\, M_{ij}\, x_j$[iii] is the scalar contraction of a 2nd-order precision tensor,[iv] ***M***, and a 1st-order tensor, ***x***. The result is a linear combination of quadratic functions formed from the products of the elements of ***x***, $x_i\, x_j$, and the corresponding elements of ***M***, M_{ij}.

In generalizing the multivariate normal distribution to a *tensor*-variate normal distribution, we seek a *tensor* analog to the quadratic form $\boldsymbol{x}^T \boldsymbol{M}\, \boldsymbol{x}$ above containing terms that are products of the elements of ***D***, $D_{ij} D_{mn}$. The most general scalar function that contains all possible linear combinations of these tensor elements is $D_{ij} A_{ijmn} D_{mn}$. In this case, $D_{ij} A_{ijmn} D_{mn}$ is a scalar contraction of the 4th-order tensor, ***A***, and the 2nd-order tensor, ***D***. The result is a linear combination of quadratic functions formed from a product of elements of ***D***, $D_{ij}\, D_{mn}$, each weighted by the corresponding element of ***A***, A_{ijmn}.

We propose the normal distribution for a 2nd-order tensor random variable, ***D***, of the form:

$$p(\boldsymbol{D}) = c\, \exp\left(-\frac{1}{2}\, D_{ij}\, A_{ijmn}\, D_{mn}\right) \text{ or}$$

$$p(\boldsymbol{D}) = c\, \exp\left(-\frac{1}{2} \sum_{i,j,m,n=1}^{3} D_{ij}\, A_{ijmn}\, D_{mn}\right) \qquad (5)$$

where ***A*** is a 4th-order precision tensor and c is the normalization constant to be determined below. The probability that a particular random tensor arises is an intrinsic property that should be independent of the coordinate system in which ***D*** is observed. The requirement

[iii] We use the Einstein summation convention, in which indices that are repeated in the expression are summed over the range of their allowable values. So, for example, $x_i\, M_{ij}\, x_j$ means $\sum_{i=1}^{3}\sum_{j=1}^{3} x_i M_{ij} x_j$.

[iv] ***M*** is usually referred to as a matrix, but it actually transforms as a 2nd-order tensor.

that $\boldsymbol{D} : \boldsymbol{A} : \boldsymbol{D}$ is a rotationally invariant quantity ensures that $\boldsymbol{A}$ is a 4th-order tensor by a simple application of the Quotient Rule Theorem.[78]

Analogies between $D_{ij}\, A_{ijmn}\, D_{mn}$ and the Elastic Strain Energy Density

The exponent in eq 5, $D_{ij}\, A_{ijmn}\, D_{mn}$, has the same form as the strain energy density, W, (e.g., see ref 79) that appears in the theory of linear elasticity.[v] Specifically, there is a direct analogy between $\boldsymbol{D}$ and the infinitesimal strain tensor, and between $\boldsymbol{A}$ and the 4th-order tensor of elastic coefficients.

In the theory of elasticity, $\boldsymbol{A}$ must be positive definite (i.e., have positive eigenvalues) to ensure that the material is elastically stable, i.e., so that stresses developed within the sample always act to return the object to a stable equilibrium configuration.[80] In this statistical application, the same requirement must apply, but for a different reason, to ensure that the variance of each component of $\boldsymbol{D}$ is positive.

The 4th-order precision tensor, $\boldsymbol{A}$, shares other properties with the tensor of elastic coefficients. $\boldsymbol{A}$ also possesses symmetries, which are reflected by its value being unaltered by the exchange of certain pairs of indices. For example, since the product of two elements of the 2nd-order tensor commutes (i.e., $D_{ij}\, D_{mn} = D_{mn}\, D_{ij}$), the position of these elements can be switched in $D_{ij}\, A_{ijmn}\, D_{mn}$ without affecting the result. Using this, we can argue that the corresponding coefficients of $\boldsymbol{A}$ should also be the same (i.e., $A_{ijmn} = A_{mnij}$). Moreover, since $\boldsymbol{D}$ is symmetric (i.e., $D_{ij} = D_{ji}$ and $D_{mn} = D_{nm}$), we require that $A_{ijmn} = A_{jimn}$ and $A_{ijmn} = A_{ijnm}$, respectively. Owing to these symmetry conditions, there are at most 21 independent elements of $\boldsymbol{A}$ that we must specify a priori[81] or estimate from sample data, rather than 81 (i.e., ref 34).

In the theory of elasticity, since W is an intrinsic property of the material, W should be independent of the coordinate system in which the components of the strain tensor are measured (e.g., see ref 81). This condition applies also to $p(\boldsymbol{D})$ as mentioned already.

The theory of elasticity also provides us with a scheme to classify 4th-order tensors of elastic coefficients according to the number, types, and degrees of symmetries they possess. The most general constitutive law of an elastic solid corresponds to *anisotropy*, requiring all 21 constants to specify the form of the tensor of elastic coefficients.[79] Other models of elastic behavior require fewer constants (e.g., see ref 79). These include the cases of *planar symmetry*, requiring 13 elastic coefficients; *orthotropy*, requiring 9 elastic coefficients; *transverse isotropy*, requiring 5 elastic coefficients; and *isotropy*, requiring only 2 elastic coefficients.

[v] W measures the internal energy stored as a homogeneous elastic body deforms.

Relationship between $\boldsymbol{A}$ and $\boldsymbol{M}$

The scalar contraction, $D_{ij}\, A_{ijmn}\, D_{mn}$, above can also be recast as a quadratic form, $\tilde{D}_r M_{rs} \tilde{D}_s$, in which the random 2nd-order tensor, $\boldsymbol{D}$, is rewritten as a 6-dimensional column vector, $\tilde{D}_r = (D_{xx}, D_{yy}, D_{zz}, D_{xy}, D_{xz}, D_{yz})$ and $\boldsymbol{M}$ has the form of the precision matrix in eq 2. An important result that is often used in continuum mechanics, and which we also exploit here, is that any 4th-order tensor, $\boldsymbol{A}$, satisfying the symmetry properties given in the previous section, can be mapped to a 6×6 symmetric matrix $\boldsymbol{M}$. Both $\boldsymbol{A}$ and $\boldsymbol{M}$ contain the same 21 independent coefficients (e.g., see refs 79, 82, 83). This correspondence allows us to write a 6×6 precision matrix, $\boldsymbol{M}$, from any 4th-order precision tensor, $\boldsymbol{A}$, and vice versa. Thus, we can construct a corresponding multivariate normal distribution directly from a tensor-variate normal distribution, as given in eq 2, when $\boldsymbol{M}$ is given by:

$$\boldsymbol{M} = \begin{pmatrix} A_{xxxx} & A_{xxyy} & A_{xxzz} & 2A_{xxxy} & 2A_{xxxz} & 2A_{xxyz} \\ A_{xxyy} & A_{yyyy} & A_{yyzz} & 2A_{yyxy} & 2A_{xzyy} & 2A_{yyyz} \\ A_{xxzz} & A_{yyzz} & A_{zzzz} & 2A_{xyzz} & 2A_{xzzz} & 2A_{yzzz} \\ 2A_{xxxy} & 2A_{xyyy} & 2A_{xyzz} & 4A_{xyxy} & 4A_{xyxz} & 4A_{xyyz} \\ 2A_{xxxz} & 2A_{xzyy} & 2A_{xzzz} & 4A_{yyxz} & 4A_{xzxz} & 4A_{xzyz} \\ 2A_{xxyz} & 2A_{yyyz} & 2A_{yzzz} & 4A_{xyyz} & 4A_{xzyz} & 4A_{yzyz} \end{pmatrix} \quad (6)$$

Using this definition, we arrive at a general form of tensor-variate normal distribution having precision tensor, $\boldsymbol{A}$, and mean tensor, $\bar{\boldsymbol{D}}$:

$$p(\boldsymbol{D}) = \frac{\sqrt{|M|}}{(2\pi)^3} \exp\left(-\frac{1}{2}\left(D_{ij} - \bar{D}_{ij}\right) A_{ijmn} \left(D_{mn} - \bar{D}_{mn}\right)\right) \quad (7)$$

The distribution in eq 7 possesses the basic form and properties of a normal distribution. Since $\boldsymbol{A}$ is positive definite, $\boldsymbol{D} : \boldsymbol{A} : \boldsymbol{D}$ is always non-negative. Moreover, $p(\boldsymbol{D})$ is always properly bounded, i.e., $1 > p(\boldsymbol{D}) \geq 0$. Also, the exponent in eq 7 is a quadratic function of the random variable (in this case, a tensor random variable) whose mean and precision tensors appear in the exponent in an analogous way to the mean vector and precision matrix of the multivariate normal distribution. In fact, we can exploit this formal correspondence to obtain many properties of the tensor-variate normal distribution by using mathematical tools and approaches that have already been developed to analyze multivariate distributions (e.g., see ref 84).

$p(\boldsymbol{D})$ When $\boldsymbol{A}$ is a General 4th-order Isotropic Tensor

We now derive the explicit form of $p(\boldsymbol{D})$ for the case in which $\boldsymbol{A}$ is a general isotropic 4th-order tensor, $\boldsymbol{A}^{iso}$.

This choice, $\boldsymbol{A} = \boldsymbol{A}^{iso}$ corresponds to the tensor of elastic coefficients for a general isotropic linearly elastic solid. In this statistical context, isotropy means that the precision tensor is rotationally invariant, i.e., its form is unchanged under any proper rotation, reflection, or inversion of coordinates in which the components of $\boldsymbol{D}$ are measured.

When $\boldsymbol{D}$ is a symmetric tensor, the most general form of $\boldsymbol{A}^{iso}$ is (e.g., see refs 81, 83):

$$A^{iso}_{ikpm} = \lambda\,\delta_{ik}\,\delta_{mp} + \mu\left(\delta_{im}\,\delta_{kp} + \delta_{ip}\,\delta_{km}\right) \qquad (8)$$

where μ and λ are as yet undetermined constants,[vi] and δ is the KronKecker delta, a 2nd-order isotropic tensor.

The scalar contraction of the exponent in the tensorvariate normal distribution, $\boldsymbol{D}:\boldsymbol{A}^{\mathrm{iso}}:\boldsymbol{D}$, becomes

$$D_{ik}\,A^{iso}_{ikpm}\,D_{pm} = D_{ik}\left(\lambda\,\delta_{ik}\,\delta_{mp} + \mu\left(\delta_{im}\,\delta_{kp} + \delta_{ip}\,\delta_{km}\right)\right)D_{pm} \qquad (9)$$

which reduces to a linear combination of two scalar invariants of $\boldsymbol{D}$, i.e.,

$$\boldsymbol{D} : \boldsymbol{A}^{iso} : \boldsymbol{D} = \lambda\,(Trace(\boldsymbol{D}))^2 + 2\mu\,Trace(\boldsymbol{D}^2) \qquad (10)$$

The distribution $p(\boldsymbol{D})$ must assume the same form under any proper rotation, reflection or inversion of laboratory coordinates because it depends only on functions of $\boldsymbol{D}$ that are rotationally invariant, Trace($\boldsymbol{D}$) and Trace($\boldsymbol{D}^2$). Thus, we find that isotropy of $\boldsymbol{A}$ implies rotational invariance of $p(\boldsymbol{D})$.

If $\boldsymbol{D}$ is a tensor whose mean is $\bar{\boldsymbol{D}}$, it is also easy to show that the tensor contraction in eq 10 becomes:

$$(\boldsymbol{D}-\bar{\boldsymbol{D}}) : \boldsymbol{A}^{iso} : \boldsymbol{D} = \lambda\,(Trace(\boldsymbol{D}-\bar{\boldsymbol{D}}))^2 + 2\mu\,Trace(\boldsymbol{D}-\bar{\boldsymbol{D}})^2) \qquad (11)$$

so that $p(\boldsymbol{D} - \bar{\boldsymbol{D}})$ is also rotationally invariant in this more general case.

To obtain the form of $p(\boldsymbol{D})$ using $\boldsymbol{A}^{iso}$ given in eq 11, we again write $\boldsymbol{D}$ as a vector, $\tilde{D} = (D_{xx}, D_{yy}, D_{zz}, D_{xy}, D_{xz}, D_{yz})^T$, and rewrite the scalar contraction in eq 11 as a quadratic form, $\tilde{D}^T\,M\,\tilde{D}$. Then, the precision matrix, $\boldsymbol{M}$, from eq 6 is sparse, having the form:

$$\boldsymbol{M} = \begin{pmatrix} \lambda+2\mu & \lambda & \lambda & 0 & 0 & 0 \\ \lambda & \lambda+2\mu & \lambda & 0 & 0 & 0 \\ \lambda & \lambda & \lambda+2\mu & 0 & 0 & 0 \\ 0 & 0 & 0 & 4\mu & 0 & 0 \\ 0 & 0 & 0 & 0 & 4\mu & 0 \\ 0 & 0 & 0 & 0 & 0 & 4\mu \end{pmatrix} = \begin{pmatrix} \Gamma & \Xi \\ \Xi^T & \Psi \end{pmatrix} \qquad (12)$$

[vi] In continuum mechanics, λ and μ correspond to the Lamé constant and shear modulus of the isotropic material, respectively.

As seen above in eq 12, $\boldsymbol{M}$ can also be written in terms of four 3×3 block matrices, Γ, Ξ, Ξ^{T}, and Ψ. Clearly, since Γ is not diagonal, the three diagonal elements of $\boldsymbol{D}$ are mutually correlated. However, the structure of Γ implies that coupling among D_{xx}, D_{yy}, and D_{zz} is independent of their size and of the particular choice of the x-, y-, and z-axes in the laboratory coordinate frame. Since $\Xi = \boldsymbol{0}$, diagonal elements of $\boldsymbol{D}$ are not correlated with off-diagonal elements of $\boldsymbol{D}$. Moreover, since $\Psi = 4\,\mu\,\boldsymbol{I}$, where $\boldsymbol{I}$ is the 3×3 identity matrix, the three off-diagonal elements of $\boldsymbol{D}$ are mutually uncorrelated, and have equal variances.

Using eq 12 in eq 7, we see that $p(\boldsymbol{D})$ can be simplified as follows:

$$p(\boldsymbol{D}) = p(D_{xx},D_{yy},D_{zz},D_{xy},D_{xz},D_{yz}) = p(D_{xx},D_{yy},D_{zz})\;p(D_{xy})\;p(D_{xz})\;p(D_{yz}) \qquad (13)$$

where

$$p(D_{xx},D_{yy},D_{zz}) = \sqrt{\frac{4\mu^2(2\mu+3\lambda)}{(2\pi)^3}} \times \exp\left(-\frac{1}{2}\left(D_{xx}-\bar{D}_{xx},D_{yy}-\bar{D}_{yy},D_{zz}-\bar{D}_{zz}\right)\right. \left.\begin{pmatrix} 2\mu+\lambda & \lambda & \lambda \\ \lambda & 2\mu+\lambda & \lambda \\ \lambda & \lambda & 2\mu+\lambda \end{pmatrix}\begin{pmatrix} D_{xx}-\bar{D}_{xx} \\ D_{yy}-\bar{D}_{yy} \\ D_{zz}-\bar{D}_{zz} \end{pmatrix}\right) \qquad (14a)$$

and

$$p(D_{xy}) = \sqrt{\frac{2\mu}{\pi}}\exp\left(-2\mu\left(D_{xy}-\bar{D}_{xy}\right)^2\right);$$

$$p(D_{xz}) = \sqrt{\frac{2\mu}{\pi}}\exp\left(-2\mu\left(D_{xz}-\bar{D}_{xz}\right)^2\right);$$

$$p(D_{yz}) = \sqrt{\frac{2\mu}{\pi}}\exp\left(-2\mu\left(D_{yz}-\bar{D}_{yz}\right)^2\right) \qquad (14b)$$

Above, the mean tensor of $\boldsymbol{D}$ is $\bar{\boldsymbol{D}}$.

Below, we use this *isotropic* form of the new tensorvariate distribution in eq 14 to obtain an analytical expression for the distribution of the eigenvalues of $\boldsymbol{D}$, and to help design optimal DT-MRI experiments.[76]

Distribution of the Eigenvalues of $\boldsymbol{D}$ for $\boldsymbol{A} = \boldsymbol{A}^{\mathrm{iso}}$

For $\boldsymbol{A} = \boldsymbol{A}^{iso}$ in eq 12 we can immediately obtain the joint probability distribution of γ_1, γ_2, and γ_3, the three

eigenvalues of $\boldsymbol{D}$. The distribution $p(\gamma_1,\gamma_2,\gamma_3)$ is a special case of $p(\boldsymbol{D})$ in eqs 14a and b, obtained by performing a principal coordinate transformation in which the three diagonal elements of $\boldsymbol{D}$ are mapped to the three eigenvalues of $\boldsymbol{D}$. Integrating over all possible values of the off-diagonal elements, and substituting γ_1, γ_2, and γ_3 for D_{xx}, D_{yy}, and D_{zz} in the distribution above, we obtain:

$$p(\gamma_1,\gamma_2,\gamma_3) = \sqrt{\frac{4\mu^2(2\mu+3\lambda)}{(2\pi)^3}}$$

$$\times \exp\left(-\frac{1}{2}\left(\gamma_1-\bar{\gamma}_1,\gamma_2-\bar{\gamma}_2,\gamma_3-\bar{\gamma}_3\right)\right.$$

$$\left.\begin{pmatrix} 2\mu+\lambda & \lambda & \lambda \\ \lambda & 2\mu+\lambda & \lambda \\ \lambda & \lambda & 2\mu+\lambda \end{pmatrix}\begin{pmatrix} \gamma_1-\bar{\gamma}_1 \\ \gamma_2-\bar{\gamma}_2 \\ \gamma_3-\bar{\gamma}_3 \end{pmatrix}\right) \quad (15)$$

where $\bar{\gamma}_1$, $\bar{\gamma}_2$, and $\bar{\gamma}_3$ are the mean eigenvalues. Equivalently, we can obtain the result in eq 15 by substituting expressions for Trace($\boldsymbol{D}-\bar{\boldsymbol{D}}$) and Trace(($\boldsymbol{D}-\bar{\boldsymbol{D}}$)^2) written in terms of γ_1, γ_2, and γ_3 into eq 13.

The joint distribution, $p(\gamma_1,\gamma_2,\gamma_3)$, in eq 15 is characterized by only two parameters, μ and λ. While the eigenvalues are correlated, their coupling is independent of their order or assignment. This finding follows because the exponent in $p(\boldsymbol{D})$, given in eq 13, depends only on (Trace($\boldsymbol{D}-\bar{\boldsymbol{D}}$))^2 and Trace(($\boldsymbol{D}-\bar{\boldsymbol{D}}$)^2), both scalar invariants of $\boldsymbol{D}$, which are inherently insensitive to the order of the eigenvalues. Thus, permuting the order of the eigenvalues will always leave this distribution unchanged.

EMPIRICAL STATISTICAL APPROACHES

Bias in Sorting the Eigenvalues of $\boldsymbol{D}$

The finding that the distribution of the eigenvalues of $\boldsymbol{D}$ is Gaussian for this particular choice of $\boldsymbol{A}$ is important. Why? Because if we design our experiment so that $\boldsymbol{A} = \boldsymbol{A}^{iso}$, then it allows us, in principle, to apply powerful parametric hypothesis tests to study the properties of the measured eigenvalues (e.g., to see if there are significant differences between them in health and disease, between eigenvalues measured in different brain regions, etc.).[76] In practice, however, there is a significant limitation in performing such hypothesis tests. We typically determine these eigenvalues from measured or simulated $\boldsymbol{D}$ data using numerical algorithms, such as the Jacobi method, or by solving the characteristic equation numerically[85] or analytically.[86] Generally, we do not know the correct assignment of γ_1, γ_2, or γ_3 beforehand; typically we sort them by size, which, in the absence of noise, would ensure that the eigenvalues are binned consistently. However, due to noise, they are not. When the sample distributions of the eigenvalues overlap, as they frequently do, there is a possibility of a misassignment. This binning or sorting error, observed for the first time in DT-MRI data by Pierpaoli and Basser,[87] introduces a bias in the sample mean of the distribution of each eigenvalue—generally, the sample mean of the largest eigenvalue is increased and the sample mean of the smallest eigenvalue is reduced.

A pernicious consequence of this sorting bias is that it artifactually reduces the standard deviation of the distribution of the eigenvalues within a Region of Interest (ROI), making the differences between the three samples appear more significant than they are. It amplifies differences among the means of the sorted eigenvalues within an ROI, making them statistically significant even in isotropic media whose "true" eigenvalues are all equal. Figure 3 shows this phenomenon in an isotropic medium. This has the effect of artifactually increasing the estimates of diffusion anisotropy such as γ_1/γ_3.[87] This artifact has also made it difficult to interpret whether differences among sorted eigenvalues measured in skeletal[88] and cardiac muscle[5] were biologically meaningful or were due to noise. Finally, the sorting bias in the eigenvalues also introduces a concomitant artifactual increase in the dispersion of the sample distribution of the three eigenvectors.[89]

Generally, when background noise is present in DWIs, it is not clear how to sort the eigenvalues and eigenvectors consistently within even a homogeneous ROI. To address this issue, we and others have developed alternative schemes for sorting eigenvalues.[89,90] The approach described below entails representing geometric and algebraic features of eigenvalue–eigenvector pairs (the former being scalars, and the latter vectors) so they can be sorted simultaneously, developing a measure of overlap between such eigenvalue–eigenvector pairs, and displaying the sorting results and artifacts graphically.[89]

The basic idea of this method came from examining the properties of the expansion of $\boldsymbol{D}$ in terms of its eigenvalues and eigenvectors, γ and $\boldsymbol{\varepsilon}$, respectively.

$$\boldsymbol{D} = \sum_{i=1}^{3} \gamma_i \varepsilon_i \varepsilon_i^T \quad (16)$$

Each term in this expansion consists of an eigenvalue, γ_i, that weights a dyadic tensor formed from the outer product of its corresponding normalized eigenvectors, $\varepsilon_i\ \varepsilon_i^T$. Each dyadic tensor, $\gamma_i\ \varepsilon_i\ \varepsilon_i^T$, is effectively a one-dimensional object, resembling a dumbbell. N.B., it is

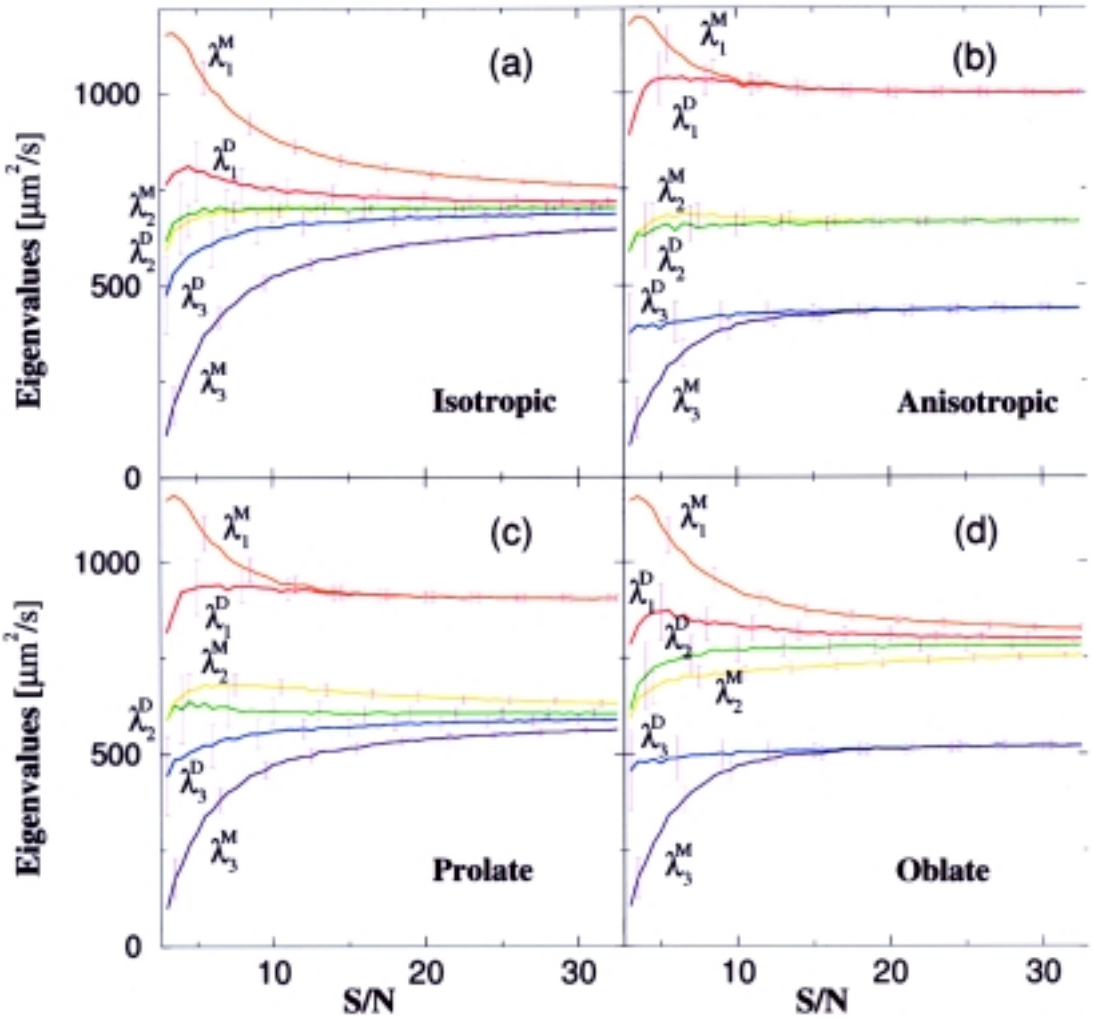

Fig. 3. Distribution of sorted eigenvalues within Regions of Interest (ROIs) having uniform diffusion properties. Eigenvalues with superscript "M" were sorted by magnitude, while those with superscript "D" were sorted as dyadic tensors. Interestingly, in all cases, magnitude sorting reduces the variance of the distribution and increases the bias in the sample means of each of the three distributions of the eigenvalues. Taken from ref 89.

not a vector with a particular *direction* (i.e., tip and tail) but a symmetric line-segment having a particular *orientation*. To display a dyadic tensor, we construct a line-segment having the length of the eigenvalue and *orientation* of its corresponding eigenvector. Each of the three eigenvalue–eigenvector dyads can then be assigned a color, Red, Green, or Blue (RGB) according to their assigned order, and can be displayed in each voxel as a 3-D object. This graphical display method, illustrated in Fig. 4, allows us to observe the effects of sorting eigenvalues and eigenvectors using different schemes.

Our strategy is to sort these dyadic pairs within an ROI in a self-consistent manner. First, we define a measure of similarity between dyads in different voxels. Just as one uses the vector dot product, "•", to determine the degree of overlap between two vectors, $\sqrt{\gamma_i}\,\varepsilon_i$ and $\sqrt{\gamma_i'}\,\varepsilon_i'$, we use the tensor dot product, "**:**", to determine the degree of overlap between two dyadic tensors constructed from them,[91] $\gamma_i\,\varepsilon_i\,\varepsilon_i^T$ and $\gamma_i'\,\varepsilon_i'\,e_i'^T$, i.e.,

$$(\gamma_i\,\varepsilon_i\,\varepsilon_i^T):(\gamma_i'\,\varepsilon_i'\,\varepsilon_i'^T) = Trace(\gamma_i\,\varepsilon_i\,\varepsilon_i^T\gamma_i'\,\varepsilon_i'\,\varepsilon_i'^T)$$
$$= \gamma_i\gamma_i'(\varepsilon_i \cdot \varepsilon_i')^2 \qquad (17)$$

We can generalize this concept to consider all three dyads simultaneously. Geometrically, this measures the degree to which two diffusion ellipsoids (whose three major axes have lengths of $\sqrt{\gamma_1}$, $\sqrt{\gamma_2}$, $\sqrt{\gamma_3}$, and $\sqrt{\gamma'}$, $\sqrt{\gamma'}$, $\sqrt{\gamma'}$, respectively) resemble each other, i.e., have similar size, shape, and orientation.[66]

The deleterious effects of magnitude sorting of the

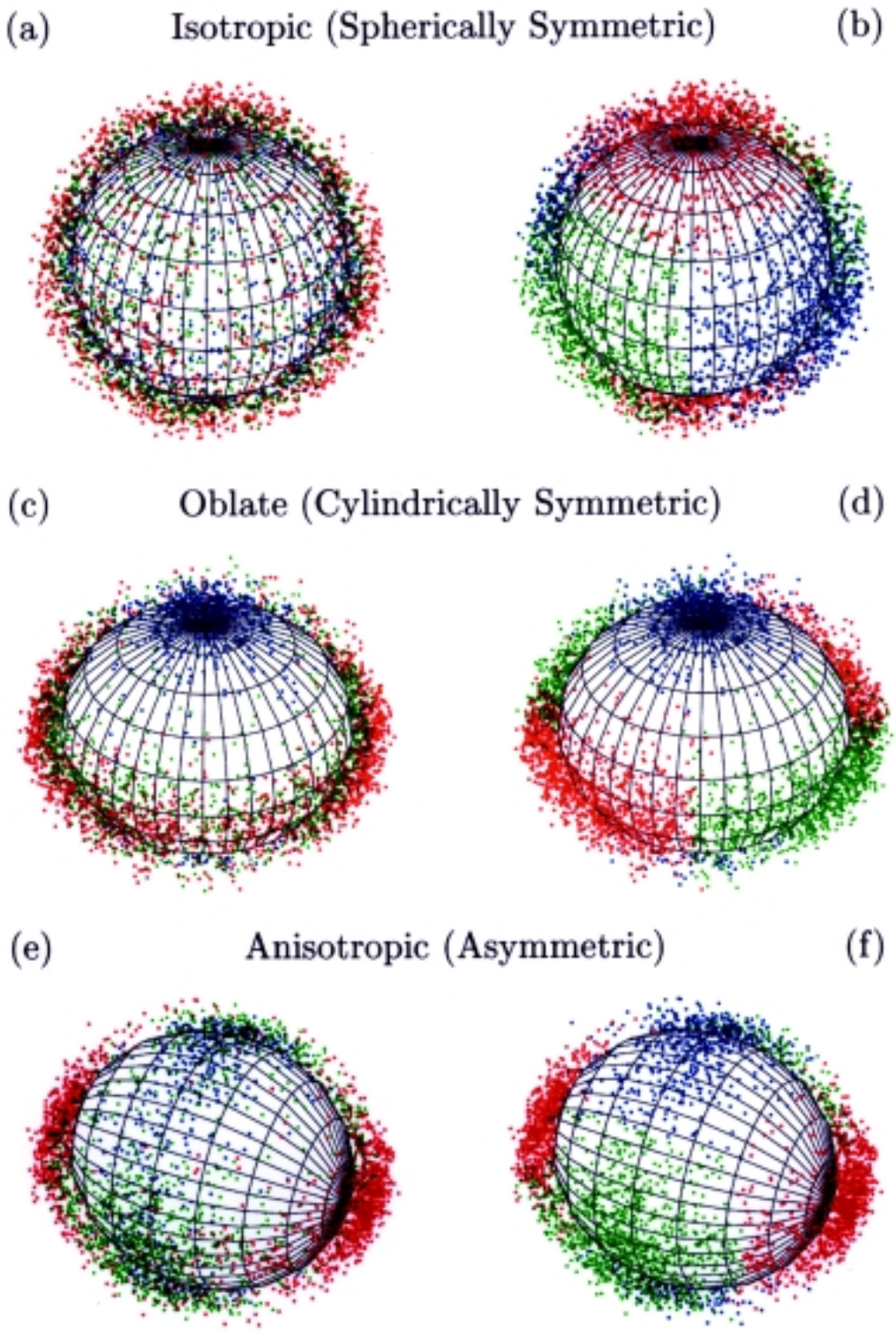

Fig. 4. Distribution of sorted dyadic tensors within ROIs having uniform diffusion properties. The three sorted eigenvalue–eigenvector pairs are displayed by the colors RGB. Magnitude sorting causes many misclassifications, as well as bias in the eigenvalues' sample mean, and in the eigenvectors' mean and variance, whereas dyadic sorting reduces these artifacts demonstrably.[89]

eigenvalues are clearly seen in Fig. 3 for isotropic and anisotropic media. Magnitude sorting clearly reduces the variance and increases the bias in the sample means of the distributions of the eigenvalues.[89] Figure 4 shows the sorted dyadic tensors encoded by RGB. This graphical display method clearly shows how magnitude sorting causes misclassifications, bias in the sample mean, and in the eigenvectors' mean and variance.[89] Figures 3 and 4 also show the improvement achieved when eigenvalues and eigenvectors are grouped and sorted together as dyadic tensors.

Scalar Invariants

One way to mitigate the effect of the sorting bias is by defining measures of diffusion anisotropy that do not depend on the ordering of the eigenvalues. The scalar invariants of the diffusion tensor are prime candidates for use in this application because they are, by definition, invariant to the permutation of the eigenvalues' order. Quantities such as the Fractional Anisotropy (FA) and the Relative Anisotropy (RA)[66,92] are functions (ratios) of scalar invariant quantities derived from $\boldsymbol{D}$. Thus, they are not susceptible to the sorting bias artifact described above. Still, they do not entirely remove the effects of noise present in DWIs. For example, both the FA and RA depend on the sample standard deviation of the estimated eigenvalues, a quantity that is inherently susceptible to the signal-to-noise ratio (SNR).[87,92]

Monte Carlo Methods to Simulate DT-MRI Experiments

Even when we know the parametric distribution of noise in diffusion tensor data, analytical estimates of errors and probability distributions cannot be calculated for most useful DT-MRI parameters since their parametric distributions cannot be derived a priori. Generally, this is because these quantities are complicated nonlinear functions of the diffusion tensor elements. In such cases we can use Monte Carlo methods. This methodology uses a parametric model of noise to explore statistical properties of any derived variables for a given simulated instance of the model.

The use of Monte Carlo (MC) methods to simulate DT-MRI is now well established. MC methods were first introduced in DT-MRI in ref 93 but were first applied by Pierpaoli and Basser to study the effect of noise on the distribution of the eigenvalues of $\boldsymbol{D}$ and on measures of diffusion anisotropy derived from $\boldsymbol{D}$.[87] As an example, Fig. 5 shows the Monte Carlo estimate of the probability density function (pdf) of the RA^2 for approximately isotropic (Fig. 5a) and anisotropic (Fig. 5b) diffusion tensors. The RA^2 scales with the variance of the estimated eigenvalues, so the pdf of RA^2 conforms to a χ^2 distribution.[74]

Matrix Perturbation Methods

Matrix perturbation methods use error-propagation analysis to approximate the uncertainty of eigenvalues and eigenvectors from an estimated matrix and its covariance matrix. They were first suggested for use in analyzing the uncertainty in diffusion tensor data in ref 94, but were elaborated upon in ref 95. The matrix perturbation approach was used to estimate the uncertainty in an eigenvalue and the width of the "cone of uncertainty" of its corresponding eigenvector from $\boldsymbol{D}$ and its covariance matrix, both of which can be estimated directly using the statistical regression procedures described in ref 1. The main shortcoming of matrix perturbation methods is that they fail in the important degenerate cases when two or three eigenvalues are similar. The former degeneracy corresponds to a diffusion process that is approximately cylindrically symmetric, and the latter to a diffusion

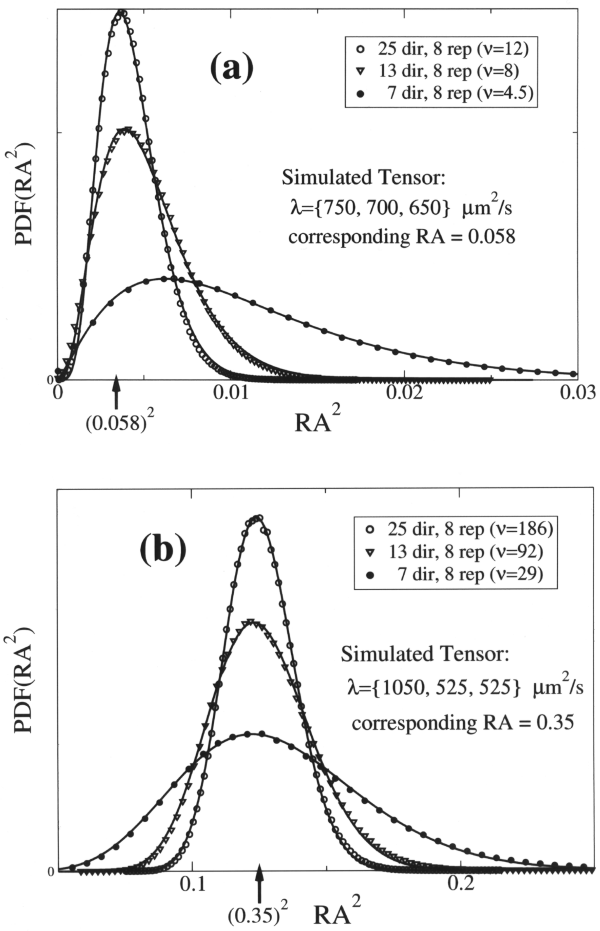

Fig. 5. Monte Carlo estimate of the probability density functions (pdf) of the RA^2 of approximately isotropic (a) and anisotropic (b) diffusion tensors. The estimated pdf conforms to a χ^2 distribution. Taken from ref 74.

process that is approximately spherically symmetric or isotropic. When one knows a priori that two or three eigenvalues are equal, it is possible to use higher-order approximations;[95] however, we generally do not have access to such foreknowledge when acquiring experimental diffusion MR data.

Bootstrap Methods

When the parametric model is known, Monte Carlo methods yield reasonable estimates of any statistic of interest. In many situations, however, parametric models do not embody the true variability observed in the measured DWI data. For example, fasciculation and bulk motion artifacts introduce additional variability in the DWI signal beyond that caused solely by RF noise. Therefore, using an empirical approach like the bootstrap is a necessity to obtain an empirical estimate of the true variability of $\boldsymbol{D}$ and any tensor-derived quantities.

As a general nonparametric approach to analyze DT-MRI data, we have proposed a particular implementation of the bootstrap method.[96,97] Bootstrap analysis is an empirical technique commonly used to obtain various uncertainty measures of a given statistic when the underlying statistical parametric model is not known a priori. Details of our implementation are given in ref 74; it is implemented by randomly drawing with replacement from the original sample of DWIs, and then obtaining sample estimates of $\boldsymbol{D}$ and any tensor-derived quantities. These estimates are used to calculate the standard errors, bias, confidence intervals, probability distributions, and other measures of uncertainty for any given statistic. The bootstrap estimate of the standard error (SE) is the nonparametric maximum likelihood estimate of the true SE. The bootstrap can also be used to determine the bias in the estimate of a given statistic. Figure 6 shows empirically-derived pdfs of RA^2 for an in vivo DT-MRI acquisition of human brain. These pdfs agree with those predicted by the parametric model for the typical isotropic (gray matter, CSF) and anisotropic (white matter) voxels (Fig. 6a–c), but deviate significantly from the expected result in one of the studied voxels (Fig. 6d).

This finding is quite useful. Deviations from the expected parametric model occur because of artifacts such as bulk motion, partial volume contamination, eddy current distortion, etc., that can make the set of DWIs inconsistent. Using the bootstrap, we can actually assess data quality on a voxel-by-voxel basis.

Continuous B-Spline Approximation of the D*-field*

We have already established that DWI measurements are inherently discrete, noisy, and voxel-averaged. However, we can view the DT-MRI data as discrete noisy samples of an underlying macroscopic diffusion tensor field, $\boldsymbol{D}(\boldsymbol{x})$, where $\boldsymbol{x} = (x, y, z)$ are the spatial coordinates in the laboratory frame of reference. This field is presumed to be continuous and smooth at a gross anatomical (voxel) length scale within many soft fibrous tissue regions, including white matter, muscles, ligaments, and tendons.

Previously, we developed a mathematical framework to estimate a continuous tensor field, $\boldsymbol{D}(\boldsymbol{x})$, from a discrete set of noisy DT-MRI measurements.[47] The method is based on obtaining a projection of the DT-MRI data onto a function space in such a way that the error norm between the sampled points and the continuous distribution is minimized. The approximated tensor field elements inherently will have a lower variance than the original measured tensor data. The reliability of these estimates improves, and bias in their means and variances is reduced when the approximated diffusion tensor field is used rather than the noisy tensor measurements themselves.

Perhaps the most important application of this new methodology is to DT-MRI fiber tractography.[2,53-65,98] Here, fiber-tract trajectories are represented as streamlines obtained by integrating the fiber direction (vector) field.[53] Integrating a noisy fiber direction vector field

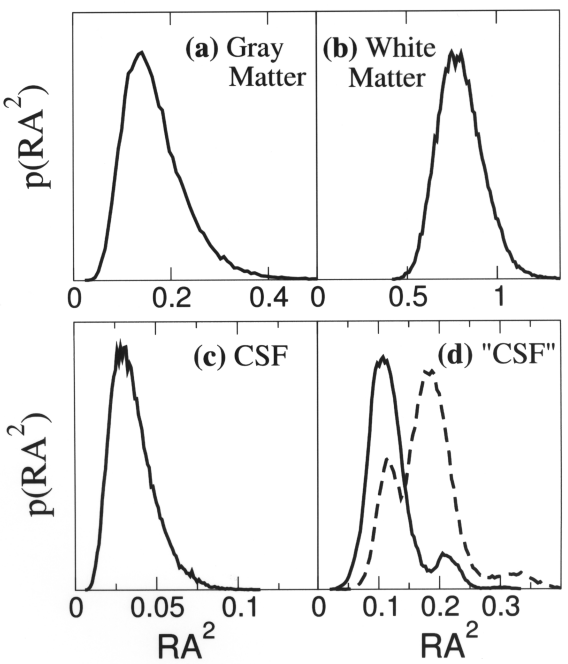

Fig. 6. Bootstrap estimates of RA^2 for an in vivo DT-MRI acquisition of human brain. Empirical estimates of the pdf are similar to those of the parametric model for typical isotropic (gray matter, CSF) and anisotropic (white matter) tissue (a,b,c). For some voxels, the measured pdf can deviate significantly from the expected parametric result (d).

can cause these computed fiber trajectories to wander off course. However, using a smoothed representation of the direction field, obtained from the continuous representation of $\boldsymbol{D}(\boldsymbol{x})$, improves the fidelity of tract-following schemes.[53]

Moreover, this method provides the basis of a unified image-processing framework for performing several generic tasks rapidly and efficiently on DT-MRI (and on other tensor field) data, including: filtering noise, sharpening edges, detecting boundaries; compressing, storing, and transmitting large image files; interpolating and extrapolating tensor data; resampling data at different resolutions; extracting textural features, segmenting images, clustering tensor data, classifying tissues; and detecting statistical outliers.

One disadvantage of this approach, however, is that it enforces continuity even in regions where there may be piece-wise discontinuities in the tensor field. For instance, across the boundary between gray matter and CSF in the brain, where Trace($\boldsymbol{D}$) (or the mean diffusivity) may jump discontinuously. Also, while there may be no appreciable change in the mean diffusivity at the boundary between gray matter and white matter, the anisotropic part (deviatoric) of $\boldsymbol{D}$ may jump.[47] In both cases, the continuous approximation smoothes over these discontinuities, introducing continuity in the field where there is none.

Wavelet Denoising of DT-MRI Data

A useful preprocessing step that can reduce noise but preserves edges or boundaries between different tissue regions is based on the wavelet transform. Despite their widespread use in other areas, however, the application of the wavelet transform and multiscale methods has been limited to diffusion MRI. A widely used wavelet denoising technique called wavelet shrinkage[99,100] can be used to estimate the true signal that is corrupted by additive, homogeneous noise. It has been applied to remove Johnson noise in the real and imaginary images in DW MR acquisitions.[101,102] We have applied wavelet shrinkage directly to the DWIs [103] since, as discussed above, in most DWI contexts, the Rician distribution is approximately Gaussian, and the bias in the estimated "true" signal for typical SNR is very small. Figure 7 compares wavelet denoising of diffusion tensor directional data in a phantom to the B-spline approximation result. It is evident that wavelet denoising preserves edges with a reduction in variability of fiber orientation comparable to that of the B-spine method.

However, these approaches are still based on the assumption that the noise is spatially homogeneous within the image, a condition that is not satisfied if artifacts other than Johnson noise are present. Thus, we have developed a new wavelet denoising strategy for spatially inhomogeneous noise, i.e., in which $\sigma = \sigma(\boldsymbol{x})$. To do this, we treat wavelet denoising as a multiple comparison problem in statistical inference.[104]

When denoising the measured data, y_i, $i = 1,\ldots,n$, which is corrupted by additive and spatially in homogeneous noise, our goal is to estimate the true signal, y_i^t below:

$$y_i = y_i^t + \sigma_i \varepsilon_i \tag{18}$$

The ε_i are random variables with zero mean and unit variance, and here we assume they are normally distributed, $N(0,1)$. Note that σ_i indicates that the noise can be different for each data point (voxel). Standard denoising using wavelet shrinkage is achieved by thresholding the wavelet coefficients d_j, $j = 1,\ldots,n$, which are related to

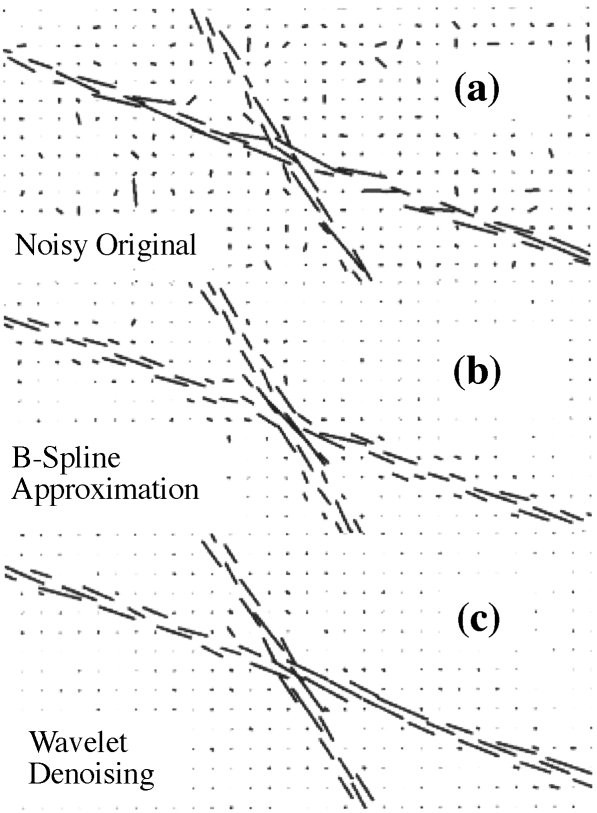

Fig. 7. Comparison of B-spline approximation and wavelet shrinkage applied to simulated DWI. Line fields of the principal diffusion orientation, with lengths proportional to the fractional anisotropy, are shown for (a) the original numerical phantom of crossing fibers (SNR = 10), (b) B-spline smoothed approximation with scale factor D = 0.6, and (c) data obtained from denoised DWIs using wavelet shrinkage with soft-threshholding. Similar improvements are observed for experimental data.

the original data, y_i, through a linear transformation:

$$d_j = \sum_i w_{ij} y_i \tag{19}$$

Since the w_{ij} are elements of an orthonormal wavelet transformation matrix, the d_j can be written in terms of the true or denoised wavelet coefficients, d_j^t, where ε_j are also $N(0,1)$:

$$d_j = d_j^t + \sigma_j \varepsilon_j \tag{20}$$

Knowing this, we can perform multiple tests of the null hypothesis, H_0: $d_j^t = 0$ against the alternative H_1:$d_j^t \neq 0$. Then, the procedure for denoising data with inhomogeneous noise properties can be performed using the following four steps.[103]

1. For each d_j find the p-value in testing H_0, $p_j = 2(1 - \Phi(d_j / \sigma_j))$ where Φ is the cumulative normal distribution.
2. To control the dissipation of statistical power of the multiple tests,[105] rank order the $|p_j|$ by increasing magnitude, $p_{(1)} \leq p_{(2)} \leq \varepsilon \leq p_{(n)}$, and find the highest rank k for which $p_{(n)} < k\alpha/n$, where a is the confidence level.[vii]
3. Threshold the j^{th} wavelet coefficient, d_j, using threshold t_j, such that $t_j = \sigma_j \Phi^{-1} (1 - p_{(k)} / 2)$. N.B. Any of the common thresholding rules can be used (e.g., soft, hard, garrote). The σ_j are calculated from the original σ_i using:

$$\sigma_j^2 = \sum_i w_{ij}^2 \sigma_i^2 \tag{21}$$

4. Use the thresholded wavelet coefficients, d_i^t, and the inverse wavelet transform, $\boldsymbol{W}^{-1}$, to obtain the denoised data, y_i^t.

This methodology is also directly applicable to denoising images of the individual components of $\boldsymbol{D}(\mathbf{x})$ (e.g., $D_{xx}(\mathbf{x})$, $D_{xy}(\mathbf{x})$). Moreover, the "noise free" coefficients, d_j^t, can be used to construct a continuous representation of $\boldsymbol{D}(\mathbf{x})$, using wavelets as the basis rather than B-splines, as described above. The most difficult task here is to obtain estimates of $\sigma_i(\mathbf{x})$. One approach is to use theoretically predicted values of $\sigma_i(\mathbf{x})$ for each component, but this assumes that we know all of the underlying sources of noise. A more robust and pragmatic approach is to obtain bootstrap estimates of $\sigma_i(\mathbf{x})$, which can be obtained readily for every voxel in the image.

[vii]Note, the parenthesis on the subscripts of the p-value indicates the rank-ordered magnitude p-statistics.

CONCLUSIONS

Many statistical analysis approaches described above are generally applicable to DWI data. This is important because several new MR displacement imaging methods do not explicitly invoke a tensor model to describe the MR signal decay. For example, Frank's HARD method produces a spherical harmonic decomposition of an ADC distribution in which diffusion gradients are sampled at high angular resolution over a sphere.[106,107] 3-D q-space MRI methods[108] are increasingly being used in biological and medical applications (e.g., see ref 109). A variant of 3-D q-space MRI called Diffusion Spectrum Imaging (DSI), recently proposed by Wedeen and Tuch et al.[110] provides features of a displacement "propagator" by performing 3-D Fourier Transforms of DW signal intensity data as a function of a 3-D pseudo q-vector. The empirical methods described in this paper are quite general and can be easily adapted to incorporate different underlying diffusion models (i.e., they are not restricted to the form of eq 1); they can also be used to model different experimental designs. Other methods, such as wavelet denoising, can be applied to the raw DWIs in an entirely model-independent way. Perhaps the only methods that specifically employ eq 1 are the parametric models. Yet, their properties are interesting to study in themselves, as they offer the possibility for optimizing DT-MRI experimental designs and for understanding the sources of variability in DT-MRI data.

We have investigated several important issues with regard to analyzing noisy DT-MRI data and designing DT-MRI experiments that are optimal in their noise immunity, at least with respect to Johnson noise. Some advances have been made in characterizing and remedying the effects of Johnson noise on the estimates of $\boldsymbol{D}$ and on other tensor-derived quantities, using a variety of parametric and nonparametric approaches described above. However, this is by no means a complete survey of statistical methodologies that can be used to extract useful information from DWI data. There are a number of new statistical approaches designed to establish anatomical connectivity between different regions, or at least establish probabilities of connections.[112–114] There are also statistical approaches being developed to determine the most parsimonious model of diffusion on a voxel-by-voxel basis.[115]

Other sources of variability must still be considered in the DWI acquisition, and these are often more difficult to characterize and correct. These include partial volume artifacts,[116–118] eddy current distortion,[119-125] physiological motion[117,126–132] (i.e., both small-scale and large-scale bulk motion), and susceptibility variations.[133–136] Typically, these effects should be corrected

as a preprocessing step, prior to denoising, by applying appropriate models. At this point, an interesting issue to address is how to ferret out useful physiological information buried in the "noise".

Acknowledgments. We wish to thank Derek Jones for carefully reading and commenting on this manuscript and Liz Salak for editing it.

REFERENCES AND NOTES

(1) Basser, P.J.; Mattiello, J.; Le Bihan, D. *J. Magn. Reson.* **1994**, *B 103*, 247–254.
(2) Basser, P.J.; Mattiello, J.; Le Bihan, D. *Biophys. J.* **1994**, *66*, 259–267.
(3) Cleveland, G.G.; Chang, D.C.; Hazlewood, C.F.; Rorschach, H.E. *Biophys. J.* **1976**, *16*, 1043–1053.
(4) Tanner, J.E. *Biophys. J.* **1979**, *28*, 107–116.
(5) Garrido, L.; Wedeen, V.J.; Kwong, K.K.; Spencer, U.M.; Kantor, H.L. *Circ. Res.* **1994**, *74*, 789–793.
(6) Moseley, M.E.; Cohen, Y.; Kucharczyk, J.; Mintorovitch, J.; Asgari, H.S.; Wendland, M.F.; Tsuruda, J.; Norman, D. *Radiology* **1990**, *176*, 439–445.
(7) Moseley, M.E.; Kucharczyk, J.; Asgari, H.S.; Norman, D. *Magn. Reson. Med.* **1991**, *19*, 321–326.
(8) Henkelman, R.M.; Stanisz, G.J.; Kim, J.K.; Bronskill, M.J. *Magn. Reson. Med.* **1994**, *32*, 592–601.
(9) Crank, J. *The Mathematics of Diffusion*, 2nd ed.; Oxford University Press: Oxford, England, 1975.
(10) Zelaya, F.; Flood, N.; Chalk, J.B.; Wang, D.; Doddrell, D. M.; Strugnell, W.; Benson, M.; Ostergaard, L.; Semple, J.; Eagle, S. *Magn. Reson. Imaging* **1999**, *17*, 331–348.
(11) Mukherjee, P.; Bahn, M.M.; McKinstry, R.C.; Shimony, J.S.; Cull, T.S.; Akbudak, E.; Snyder, A.Z.; Conturo, T.E. *Radiology* **2000**, *215*, 211–220.
(12) Sotak, C.H. *NMR Biomed.* **2002**, *15*, 561–569.
(13) Jones, D.K.; Lythgoe, D.; Horsfield, M.A.; Simmons, A.; Williams, S.C.; Markus, H.S. *Stroke* **1999**, *30*, 393–397.
(14) Horsfield, M.A.; Jones, D.K. *NMR Biomed.* **2002**, *15*, 570–577.
(15) Rose, S.E.; Chen, F.; Chalk, J.B.; Zelaya, F.O.; Strugnell, W.E.; Benson, M.; Semple, J.; Doddrell, D.M. *J. Neurol. Neurosurg. Psychiatry* **2000**, *69*, 528–530.
(16) Ellis, C.M.; Simmons, A.; Jones, D.K.; Bland, J.; Dawson, J.M.; Horsfield, M.A.; Williams, S.C.; Leigh, P.N. *Neurology* **1999**, *53*, 1051–1058.
(17) Glauche, V.; Sach, M.; Koch, M.; Winkler, G.; Nolte, U.; Finsterbusch, J.; Frahm, J.; Weiller, C.; Buchel, C. *Neuroimage* **2001**, *13*, S128.
(18) Hedehus, M.; Sullivann, E.V.; de Crespigny, A.; Moseley, M.E.; Lim, K.; Pfefferbaum, A. ISMRM, Philadelphia, 1999; p 932.
(19) Pfefferbaum, A.; Sullivan, E.V. *Neuroimage* **2002**, *15*, 708–718.
(20) Klingberg, T.; Hedehus, M.; Temple, E.; Salz, T.; Gabrieli, J.D.; Moseley, M.E.; Poldrack, R.A. *Neuron* **2000**, *25*, 493–500.
(21) Rugg-Gunn, F.J.; Eriksson, S.H.; Symms, M.R.; Barker, G.J.; Duncan, J.S. *Brain* **2001**, *124*, 627–636.
(22) Eriksson, S.H.; Rugg-Gunn, F.J.; Symms, M.R.; Barker, G.J.; Duncan, J.S. *Brain* **2001**, *124*, 617–626.
(23) Filippi, C.G.; Ulug, A.M.; Ryan, E.; Ferrando, S.J.; van Gorp, W. *Am. J. Neuroradiol.* **2001**, *22*, 277–283.
(24) Pomara, N.; Crandall, D.T.; Choi, S.J.; Johnson, G.; Lim, K.O. *Psychiatry Res.* **2001**, *106*, 15–24.
(25) Buchsbaum, M.S.; Tang, C.Y.; Peled, S.; Gudbjartsson, H.; Lu, D.; Hazlett, E.A.; Downhill, J.; Haznedar, M.; Fallon, J.H.; Atlas, S. W. *Neuroreport* **1998**, *9*, 425–430.
(26) Lim, K.O.; Hedehus, M.; Moseley, M.; de Crespigny, A.; Sullivan, E.V.; Pfefferbaum, A. *Arch. Gen. Psychiatry* **1999**, *56*, 367–374.
(27) Sinha, S.; Bastin, M.E.; Whittle, I.R.; Wardlaw, J.M. *Am. J. Neuroradiol.* **2002**, *23*, 520–527.
(28) Mori, S.; Frederiksen, K.; van Zijl, P. C.; Stieltjes, B.; Kraut, M.A.; Solaiyappan, M.; Pomper, M.G. *Ann. Neurol.* **2002**, *51*, 377–380.
(29) Pierpaoli, C.; Barnett, A.; Pajevic, S.; Chen, R.; Penix, L.; Virta, A.; Basser, P.J. *Neuroimage* **2001**, *13*, 1174–1185.
(30) Huppi, P.S.; Maier, S.E.; Peled, S.; Zientara, G.P.; Barnes, P.D.; Jolesz, F.A.; Volpe, J.J. *Pediatr. Res.* **1998**, *44*, 584–590.
(31) Neil, J.J.; Shiran, S.I.; McKinstry, R.C.; Schefft, G.L.; Snyder, A.Z.; Almli, C.R.; Akbudak, E.; Aronovitz, J.A.; Miller, J.P.; Lee, B.C.; Conturo, T.E. *Radiology* **1998**, *209*, 57–66.
(32) Klingberg, T.; Vaidya, C.J.; Gabrieli, J.D.; Moseley, M.E.; Hedehus, M. *Neuroreport* **1999**, *10*, 2817–2821.
(33) Pfefferbaum, A.; Sullivan, E.V.; Hedehus, M.; Lim, K.O.; Adalsteinsson, E.; Moseley, M. *Magn. Reson. Med.* **2000**, *44*, 259–268.
(34) Sullivan, E.V.; Adalsteinsson, E.; Hedehus, M.; Ju, C.; Moseley, M.; Lim, K.O.; Pfefferbaum, A. *Neuroreport* **2001**, *12*, 99–104.
(35) Nusbaum, A.O.; Tang, C.Y.; Buchsbaum, M.S.; Wei, T.C.; Atlas, S. W. *Am. J. Neuroradiol.* **2001**, *22*, 136–142.
(36) Torrey, H.C. *Phys. Rev.* **1956**, *104*, 563–565.
(37) Bloch, F. *Phys. Rev.* **1946**, *70*, 460–474.
(38) Douglass, D.C.; McCall, D.W. *J. Phys. Chem.* **1958**, *62*, 1102.
(39) Stejskal, E.O. *J. Chem. Phys.* **1965**, *43*, 3597–3603.
(40) Wayne, R.C.; Cotts, R. M. *Phys. Rev.* **1966**, *151*, 264–272.
(41) Neuman, C.H. *J. Chem. Phys.* **1974**, *60*, 4508–4511.
(42) Stejskal, E.O.; Tanner, J. E. *J. Chem. Phys.* **1965**, *42*, 288–292.
(43) Tanner, J.E. *J. Chem. Phys.* **1978**, *69*, 1748–1754.
(44) Mattiello, J.; Basser, P.J.; Le Bihan, D. *J. Magn. Reson.* **1994**, *A 108*, 131–141.
(45) Mattiello, J.; Basser, P.J.; Le Bihan, D. In *Diffusion and Perfusion Magnetic Resonance Imaging*; Bihan, D.L.,

Ed.; Raven Press: New York, 1995.
(46) Mattiello, J.; Basser, P.J.; Le Bihan, D. *Magn. Reson. Med.* **1997**, *37*, 292–300.
(47) Pajevic, S.; Aldroubi, A.; Basser, P.J. *J. Magn. Reson.* **2002**, *154*, 85–100.
(48) Basser, P.J.; Le Bihan, D. 11th Annual Meeting of the SMRM, Berlin, 1992; p 1221.
(49) Jones, D.K.; Williams, S.C.R.; Horsfield, M.A. 5th Annual Meeting of the ISMRM, Vancouver, 1997; p 1743.
(50) Pierpaoli, C. 5th Annual Meeting of the ISMRM, Vancouver, 1997; p 1741.
(51) Pajevic, S.; Pierpaoli, C. *Magn. Reson. Med.* **1999**, *42*, 526–40.
(52) Makris, N.; Worth, A.J.; Sorensen, A.G.; Papadimitriou, G.M.; Wu, O.; Reese, T.G.; Wedeen, V.J.; Davis, T.L.; Stakes, J.W.; Caviness, V.S.; Kaplan, E.; Rosen, B.R.; Pandya, D.N.; Kennedy, D.N. *Ann. Neurol.* **1997**, *42*, 951–962.
(53) Basser, P.J.; Pajevic, S.; Pierpaoli, C.; Duda, J.; Aldroubi, A. *Magn. Reson. Med.* **2000**, *44*, 625–632.
(54) Basser, P.J. 6th Annual Meeting of the ISMRM, Sydney, 1998; p 1226.
(55) Wedeen, V.J.; Davis, T.L.; Weisskoff, R.M.; Tootell, R.; Rosen, B.R.; Belliveau, J.W. Proceedings of the First International Conference for Functional Mapping of the Human Brain, Paris, 1995; p P1.36.
(56) Wedeen, V.J. 2nd Brain Map Meeting, Boston, 1996; p P1A4–021.
(57) Conturo, T.E.; Lori, N.F.; Cull, T.S.; Akbudak, E.; Snyder, A.Z.; Shimony, J.S.; McKinstry, R.C.; Burton, H.; Raichle, M.E. *Proc. Natl. Acad. Sci. USA* **1999**, *96*, 10422–10427.
(58) Jones, D.K.; Simmons, A.; Williams, S.C.R.; Horsfield, M.A. 6th Annual Meeting of the ISMRM, Sydney, 1998; p 531.
(59) Jones, D.K.; Simmons, A.; Williams, S.C.; Horsfield, M.A. *Magn. Reson. Med.* **1999**, *42*, 37–41.
(60) Mori, S.; Crain, B.J.; Chacko, V.P.; van Zijl, P.C. *Ann. Neurol.* **1999**, *45*, 265–269.
(61) Mori, S.; Xue, R.; Crain, B.; Solaiyappan, M.; Chacko, V.P.; Zijl, P.C.M.v. 7th Annual Meeting of the ISMRM, Philadelphia, 1999; p 320.
(62) Mori, S.; Kaufmann, W.E.; Pearlson, G.D.; Crain, B.J.; Stieltjes, B.; Solaiyappan, M.; van Zijl, P.C. *Ann. Neurol.* **2000**, *47*, 412–414.
(63) Poupon, C.; Mangin, J.-F.; Frouin, V.; Regis, F.; Poupon, C.; Pachot-Clouard, M.; Le Bihan, D.; Bloch, I. Proceedings of MICCAI'98, 1998; pp 489–498.
(64) Poupon, C.; Clark, C.A.; Frouin, V.; Bloch, I.; Le Bihan, D.; Mangin, J.-F. 8th Annual Meeting of the ISMRM, Philadelphia, 1999; pp 325.
(65) Poupon, C.; Mangin, J.; Clark, C.A.; Frouin, V.; Regis, J.; Le Bihan, D.; Bloch, I. *Med. Image. Anal.* **2001**, *5*, 1–15.
(66) Basser, P.J. *NMR Biomed.* **1995**, *8*, 333–344.
(67) Le Bihan, D. *Diffusion and Perfusion Magnetic Resonance Imaging*; Raven Press: New York, 1995.
(68) Basser, P.J. *Ann. NY Acad. Sci.* **1997**, *820*, 123–138.
(69) Mori, S.; Barker, P.B. *Anat. Rec.* **1999**, *257*, 102–109.
(70) Le Bihan, D.; Mangin, J.F.; Poupon, C.; Clark, C.A.; Pappata, S.; Molko, N.; Chabriat, H. *J. Magn. Reson. Imaging* **2001**, *13*, 534–546.
(71) Basser, P.J.; Jones, D.K. *NMR Biomed.* **2002**, *15*, 456–467.
(72) Henkelman, R.M. *Med. Phys.* **1985**, *12*, 232–233.
(73) Gudbjartsson, H.; Patz, S. *Magn. Reson. Med.* **1995**, *34*, 910–914.
(74) Pajevic, S.; Basser, P.J. *J. Magn. Reson.* **2003**, *161(1)*, 1–14.
(75) Basser, P. J.; Pajevic, S. 7th Annual Meeting of the ISMRM, Philadelphia, 1999; p 1789.
(76) Basser, P.J.; Pajevic, S. IEEE Trans. Med. Imaging **2003**, *22(7)*, 785–794.
(77) *Introduction to Statistical Pattern Recognition*; Fukunaga, K., Ed.; Academic Press: New York, 1972.
(78) Arfken, G.B.; Weber, H.-J. Mathematical Methods for Physicists, 5th ed.; Harcourt/Academic Press: New York, 2000.
(79) Green, A.E.; Zerna, W. Theoretical Elasticity, 2nd ed.; Oxford University Press: London, 1954.
(80) Malvern, L.E. *Introduction to the Mechanics of a Continuous Medium*; Prentice-Hall: Englewood Cliffs, NJ, 1969.
(81) Jeffreys, H. *Cartesian Tensors*; Cambridge University Press: Cambridge, 1931.
(82) Onat, E.T.; Boehler, J.P.; A.A. Kirillov, J. *J. Elasticity* **1994**, 97–110.
(83) Zheng, Q.S. *Z. Angew. Math. Mech.* **1994**, *74*, 357–359.
(84) Anderson, T.W. *An Introduction to Multivariate Statistics*; 2nd ed.; John Wiley & Sons: New York, 1984.
(85) Press, W.H.; Teukolsky, S.A.; Vetterling, W.T.; Flannery, B.P. *Numerical Recipes in C*, 2nd ed.; Cambridge University Press: Cambridge, 1992.
(86) Hasan, K.M.; Basser, P.J.; Parker, D.L.; Alexander, A. L. *J. Magn. Reson.* **2001**, *152*, 41–47.
(87) Pierpaoli, C.; Basser, P.J. *Magn. Reson. Med.* **1996**, *36*, 893–906.
(88) Hsu, E.W.; Mori, S. *Magn. Reson. Med.* **1995**, *32*, 194–200.
(89) Basser, P.J.; Pajevic, S. *Magn. Reson. Med.* **2000**, *44*, 41–50.
(90) Martin, K.M.; Papadakis, N.G.; Huang, C.L.; Hall, L.D.; Carpenter, T.A. *Magn. Reson. Imaging* **1999**, *17*, 893–901.
(91) Morse, P.M.; Feschbach, H. *Methods of Theoretical Physics*; McGraw-Hill: New York, 1953.
(92) Basser, P.J.; Pierpaoli, C. *J. Magn. Reson. B* **1996**, *111*, 209–219.
(93) Basser, P.J.; Mattiello, J.; Le Bihan, D.; NIH, assignee. Method and System for Measuring the Diffusion Tensor and for Diffusion Tensor Imaging. U.S. Patent 5,539,310. July 23, 1996.
(94) Basser, P.J. 5th Annual Meeting of the ISMRM, Vancouver, 1997; p 1740.
(95) Anderson, A.W. *Magn. Reson. Med.* **2001**, *46*, 1174–1188.

(96) Efron, B. *An Introduction to the Bootstrap*; Chapman & Hall: New York, 1993.
(97) Efron, B. *Ann. Statist.* **1979**, *7*, 1–26.
(98) Mori, S.; Crain, B.J.; van Zijl, P.C. Proceedings of International Conference on Functional Mapping of the Human Brain, Montreal, 1998.
(99) Donoho, D.L. *IEEE Trans. Inform. Theory* **1995**, *41*, 613–627.
(100) Donoho, D.L.; Johnstone, I.M. *Biometrika* **1994**, *81*, 425–455.
(101) Nevo, U. ISMRM Conference "Diffusion MRI: Biophysical Issues (What can we measure?)", St. Malo, France, 2002.
(102) Nevo, U. Bat Sheva Workshop on Diffusion, Tel Aviv, 2001.
(103) Pajevic, S.; Basser, P.J.; Rohde, G.; Pierpaoli, C.; Jones, D.K.; Aldroubi, A. 11th Annual Meeting of the ISMRM, Honolulu, 2002; p 1176.
(104) Vidakovic, B. *Statistical Modelling by Wavelets*; John Wiley & Sons: New York, 1999.
(105) Abramovich, F.; Benjamini, Y. *Comput. Statist. Data Anal.* **1996**, *22*, 351–361.
(106) Frank, L.R. *Magn. Reson. Med.* **2001**, *45*, 935–939.
(107) Frank, L.R. *Magn. Reson. Med.* **2002**, *47*, 1083–1099.
(108) Callaghan, P.T. *Principles of Nuclear Magnetic Resonance Microscopy*; Oxford University Press: Oxford, 1991.
(109) Assaf, Y.; Mayk, A.; Cohen, Y. *Magn. Reson. Med.* **2000**, *44*, 713–722.
(110) Wedeen, V.J.; Reese, T.G.; Tuch, D.S.; Weigel, M. R.; Dou, J.-G.; Weiskoff, R. M.; Chessler, D. 10th Annual Meeting of ISMRM, Denver, 2000; p 82.
(111) Tuch, D.S.; Weiskoff, R.M.; Belliveau, J.W.; Wedeen, V.J. 9th Annual Meeting of ISMRM, Philadelphia, 1999; p 321.
(112) Behrens, T.E.J.; Jenkinson, M.; Brady, J.M.; Smith, S.M. 11th Annual Meeting of the ISMRM, Honolulu, 2002; p 1142.
(113) Behrens, T.E.J.; Woolrich, M.; Jenkinson, M.; Brady, J.M.; Smith, S.M. 11th Annual Meeting of the ISMRM, Honolulu, 2002; p 1160.
(114) Tuch, D.S.; Wiegell, M.R.; Reese, T.G.; Belliveau, J.W.; Wedeen, V.J. 10th Annual Meeting of ISMRM, Glasgow, 2001; p 502.
(115) Shrager, R.I.; Jones, D.K.; Pajevic, S.; Munson, P.; Basser, P.J. ISMRM Conference "Diffusion MRI: Biophysical Issues (What can we measure?)", St. Malo, France, 2002.
(116) Alexander, A.L.; Hasan, K.M.; Lazar, M.; Tsuruda, J.S.; Parker, D.L. *Magn. Reson. Med.* **2001**, *45*, 770–780.
(117) Conturo, T.E.; McKinstry, R.C.; Aronovitz, J.A.; Neil, J.J. *NMR Biomed.* **1995**, *8*, 307–832.
(118) Papadakis, N.G.; Martin, K.M.; Mustafa, M.H.; Wilkinson, I.D.; Griffiths, P.D.; Huang, C.L.; Woodruff, P.W. *Magn. Reson. Med.* **2002**, *48*, 394–398.
(119) Koch, M.; Norris, D.G. *Phys. Med. Biol.* **2000**, *45*, 3821–3832.
(120) Horsfield, M.A. *Magn. Reson. Imag.* **1999**, *17*, 1335–1345.
(121) Haselgrove, J.C.; Moore, J. R. *Magn. Reson. Med.* **1996**, *36*, 960–964.
(122) Jezzard, P.; Balaban, R.S. *Magn. Reson. Med.* **1995**, *34*, 65–73.
(123) Calamante, F.; Porter, D.A.; Gadian, D.G.; Connelly, A. *Magn. Reson. Med.* **1999**, *41*, 95–102.
(124) Bastin, M.E. *Magn. Reson. Imaging* **1999**, *17*, 1011–24.
(125) Mangin, J.F.; Poupon, C.; Clark, C.; Le Bihan, D.; Bloch, I. *Med. Image Anal.* **2002**, *6*, 191–198.
(126) Chien, D.; Buxton, R.B.; Kwong, K.K.; Brady, T.J.; Rosen, B.R. *J. Comput. Assist. Tomogr.* **1990**, *14*, 514–520.
(127) Enzmann, D.R.; Pelc, N.J. *Radiology* **1992**, *185*, 653–660.
(128) Poncelet, B.P.; Wedeen, V.J.; Weisskoff, R.M.; Cohen, M.S. *Radiology* **1992**, *185*, 645–651.
(129) Turner, R.; Le Bihan, D.; Maier, J.; Vavrek, R.; Hedges, L.K.; Pekar, J. *Radiology* **1990**, *177*, 407–414.
(130) Dietrich, O.; Heiland, S.; Benner, T.; Sartor, K. *Neuroradiology* **2000**, *42*, 85–91.
(131) Skare, S.; Andersson, J.L. *Magn. Reson. Imaging* **2001**, *19*, 1125–1128.
(132) Norris, D.G. *J. Magn. Reson. Imaging* **2001**, *13*, 486–495.
(133) Koch, M.A.; Glauche, V.; Finsterbusch, J.; Nolte, U. G.; Frahm, J.; Weiller, C.; Buchel, C. *Neuroimage* **2002**, *17*, 497–506.
(134) Sener, R.N. *Clin. Imaging* **2002**, *26*, 371–374.
(135) Nolte, U.G.; Finsterbusch, J.; Frahm, J. *Magn. Reson. Med.* **2000**, *44*, 731–736.
(136) Brockstedt, S.; Moore, J.R.; Thomsen, C.; Holtas, S.; Stahlberg, F. *Magn. Reson. Imaging* **2000**, *18*, 649–657.